



Plasma-induced methane catalytic cracking: Effects of experimental conditions

Shizhang Wang^a, Junjie Wang^a, Dongdong Feng^{a,*}, Fuhua Wang^b, Yijun Zhao^a, Shaozeng Sun^a

^a School of Energy Science and Engineering, Harbin Institute of Technology, Harbin, 150001, China

^b Acre Coking & Refractory Engineering Consulting Corporation, Mcc, Dalian, 116000, China

ARTICLE INFO

Handling Editor: Dr M Mahdi Najafpour

Keywords:

CH₄ cracking

H₂

Plasma

Carbon black

ABSTRACT

Low-carbon conversion of hydrocarbon fuels and feedstocks, as well as the macroscopic production of H₂, are central focus in the advancement of high-value and efficient conversion of CH₄. The effects of Ar addition ratio, discharge power and temperature on the results of plasma methane cracking were investigated on a dielectric barrier discharge (DBD) plasma experimental system. The results show that the addition of Ar can improve the methane conversion, and the optimal ratio of CH₄ conversion to H₂ production after the effect is CH₄: Ar = 1:1, at which the methane conversion reaches 49.62% and the H₂ selectivity reaches 52.66%. The plasma at 25 °C can make the methane conversion close to the effect of catalytic cracking at 600 °C, while the H₂ selectivity is lower, the H₂ generation is 32.59% lower than the latter, and the products have more C₂–C₄ hydrocarbon impurities. The solid byproduct resulting from the DBD plasma cracking of methane primarily consisted of carbon black, possessing an average particle size of 62.21 nm. The incorporation of Ar and the amplification of power augment the CH^{*} radical intensities, which suggests both conditions contribute positively to the dissociation of the CH₄ molecule.

1. Introduction

Hydrogen energy has been integrated into the new energy storage and utilization paradigm in the twenty-first century. Achieving low-carbon energy planning and the efficient development and utilization of hydrogen energy requires addressing the key challenges of clean and efficient production of H₂, as well as high-density storage through innovative technological means. The primary source of H₂ is currently fossil energy [1], with the most significant energy efficiency of 83% achieved in the production of hydrogen from natural gas (CH₄ as the main component) [2]. Furthermore, the successful promotion of the China-Russia East Natural Gas Pipeline [3] will annually introduce 38 billion m³ of clean natural gas, presenting Heilongjiang with both the task and opportunity of CH₄ conversion and transportation as the “bridgehead” of the East Pipeline.

Low-temperature plasma technology is an emerging method that leverages reactants in a low-temperature plasma state, where high-energy electrons are excited or ionized in an electric field, enabling the occurrence of chemical reactions that are otherwise difficult under normal conditions. This technology aims to facilitate the molecular

reforming of reactants. Research has demonstrated that plasma technology has the capability to transform natural gas into high-value fuels, including hydrogen, syngas, and C₂ hydrocarbons. Plasma-catalyzed methane conversion is particularly advantageous at 25 °C. The mechanism governing low-temperature plasma-catalyzed methane conversion is primarily influenced by the scavenging of ions or free radicals, rather than ionic reactions [4]. This technology can directly excite, dissociate, and ionize CH₄ molecules at relatively low temperatures [5,6], leading to the generation of numerous free radicals and other reactive species [7–10], ultimately enabling highly efficient activation and conversion of CH₄. Low-temperature plasma technology offers several advantages, including high chemical activity, low energy consumption, and rapid activation and deactivation. Various plasma discharge systems, such as spark discharge [11,12], dielectric barrier discharge (DBD) [13], sliding arc discharge (GAD) [14], radio frequency (RF) discharge [15], microwave (MW) discharge [16], and corona discharge (CD) [17], have been employed for the conversion of CH₄. This technology presents a low-energy method for converting natural gas into valuable fuels, such as hydrogen, syngas, and C₂ hydrocarbons.

The dielectric barrier discharge (DBD) method is a prevalent form of

* Corresponding author.

E-mail addresses: 18846780639@163.com (S. Wang), wangjunjie12138@126.com (J. Wang), 08031175@163.com (D. Feng), 21S002019@stu.hit.edu.cn (F. Wang), zhaoyijun@hit.edu.cn (Y. Zhao), sunzs@hit.edu.cn (S. Sun).

<https://doi.org/10.1016/j.ijhydene.2024.03.178>

Received 7 February 2024; Received in revised form 4 March 2024; Accepted 13 March 2024

Available online 19 March 2024

0360-3199/© 2024 Hydrogen Energy Publications LLC. Published by Elsevier Ltd. All rights reserved.

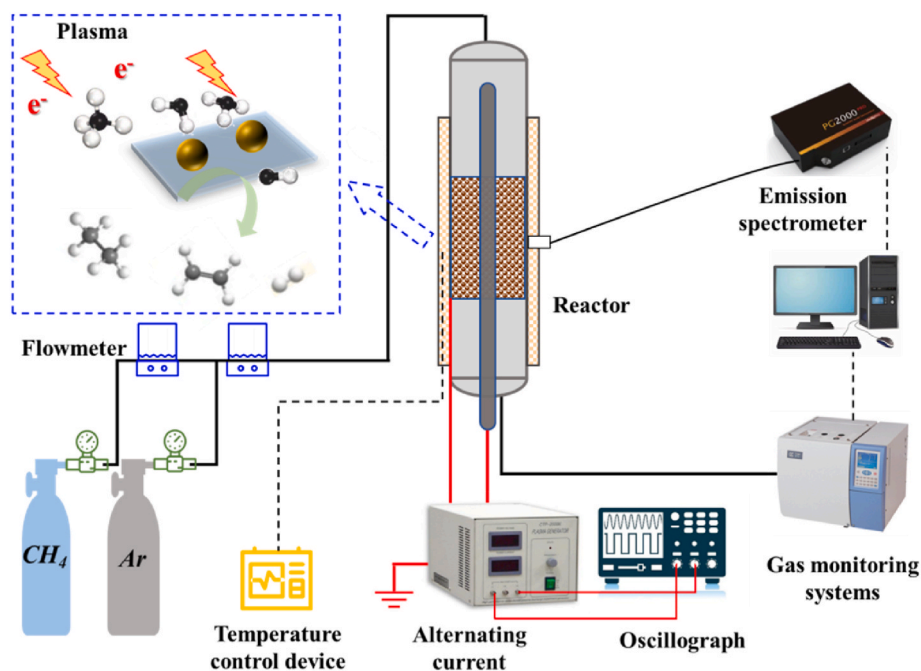


Fig. 1. Diagram of catalytic cracking reaction of methane.

low-temperature plasma used extensively in methane conversion research. DBD is characterized by numerous micro-discharge filamentary channels [18], with electron temperatures ranging from 1 to 10 eV [19,20]. This electron temperature is adequate for the activation of stable gas molecules such as CH₄, CO₂, O₂, and H₂O [21–24]. Despite the high electron density in the micro-discharge channels, approximately 10^{12} to 10^{15} cm⁻³ [25,26], the average electron density in the gaps between the discharge channels is low. The CH₄ conversion using this method is relatively low, resulting in primarily hydrocarbons with carbon numbers ranging from 2 to 4, and also some with carbon numbers up to 5 [27]. Among the products, C₂H₆ exhibits the highest selectivity, reaching close to 50%; however, the selectivity decreases significantly as the carbon number increases. Furthermore, an increase in the residence time of methane molecules in the discharge region leads to a gradual rise in CH₄ conversion and H₂ selectivity, reaching a maximum value and then stabilizing [28]. The prevailing understanding in the current literature regarding the mechanism of methane activation by dielectric-blocked discharge plasma suggests that the methane molecule undergoes dissociation of the C–H bond in the presence of electrons [29], leading to the formation of three radicals, namely CH₃^{*}, CH₂^{*}, and CH^{*}. Simulations indicate that the relative quantitative relationships of these three radicals are 79%, 15%, and 5% [30]. CH₃^{*} is regarded as the most critical species due to its absolute numerical dominance.

Despite considerable strides, numerous challenges remain in the comprehension of electron activation pathways. Most prevailing transient detection methods are inept at functioning under discharge conditions, limited by the small number of in-situ plasma diagnostic tools available, such as emission spectroscopy. These tools demonstrate a potential to detect CH^{*} radicals, but their capability does not extend to CH₃^{*} and CH₂^{*}. Subsequently, the irrefutable experimental evidence for an electron activation pathway continues to pose a challenge. Moreover, the process of methane activation whether it takes place in a singular step or via the intermediate CH₃^{*} and CH₂^{*} remains ambiguous. Undoubtedly, the instrumental role of electrons in dielectric barrier discharges for methane activation is emphasized by the incapacity of the cold plasma, generated by these discharges, to activate methane thermally.

This research investigates the conversion of CH₄ into H₂ induced by DBD low-temperature plasma. Discharge experiments were conducted at

constant and variable temperatures in quartz and corundum reactors under ambient and controlled temperature conditions. The study aims to analyze how the plasma discharge power, CH₄/Ar concentration ratio, flow rate, and discharge temperature affect the reaction under standard atmospheric pressure. Spectral analysis is utilized to examine the distribution characteristics of intermediate free radicals generated from methane cracking reactions under plasma conditions. By combining macroscopic and microscopic viewpoints, we elucidate the evolving pathway of the methane cracking reaction under different reaction conditions. This approach leads to the identification of an optimal operational configuration for methane cracking employing medium-blocking discharge plasma. Furthermore, a comprehensive analysis was conducted on the structure and properties of the reacted solid-phase products, taking into full account the economic aspect of plasma-induced methane technology, which carries crucial implications for its further application.

2. Experimental and characterization methods

2.1. Experimental system

Methane cracking experiments were carried out using dielectric blocking discharge plasma, and the experimental system is shown in Fig. 1, which consists of three parts: the discharge and detection system, the gas distribution system and the measurement system.

Discharge system: The experimental setup includes a CTP-2000K low-temperature plasma power supply, a voltage regulator, a coaxial DBD reactor, and a TBS1102C oscilloscope. The plasma power supply generates high-voltage alternating current with one high-voltage output terminal and two low-voltage output terminals (having 0.47 μF capacitance and 50 Ω resistor sampling, respectively), which are connected to the corresponding electrodes of the reactor through wiring. The reactor is comprised of a stainless-steel high-voltage electrode with a body diameter of 10 mm and a sawtooth diameter of 14 mm. It also includes a quartz/corundum tube with an outer diameter of 25 mm and an inner diameter of 20 mm, and an external ground electrode (wire mesh) with a discharge gap of 3 mm. The discharge area has a length of approximately 15 cm, and the heater's heated area spans about 20 cm, encompassing the discharge area.

Measurement systems: The measurement system is comprised of a gas chromatograph (GC7900) for analyzing gaseous products and a spectrometer (PG2000-Pro-EX) for assessing intermediate state products. The reactor's outlet gas is routed to the GC7900 gas inlet via a pipeline. Equipped with a hydrogen flame detector (FID) and a thermal conductivity detector (TCD), the GC7900 enables online detection of C₁–C₄ hydrocarbon products by the FID and H₂ in the products by the TCD. The fiber optic measurement system comprises an optical fiber and a spectrometer. The fiber optic probe is aligned with the measuring point on the reactor, transmitting signals to the spectrometer. This spectrometer features a 10 μm slit, a detection wavelength range of 195 nm–1115 nm, and a resolution of 1.18 nm, enabling the detection of luminescent signals from free radicals within this range.

2.2. Experimental operations and test methods

Operation method: Prior to the experiment, the gas chromatograph was activated after being filled with carrier gas and left to allow the detector baseline to stabilize. Following the connection of electrodes and the gas circuit, methane and argon were passed through, with the total flow rate of the two being maintained at 30 sccm. The reactor is purged of air as the gas is continuously expelled for a duration of 30 min. Following this, the gas composition is rigorously monitored at two separate 5-min intervals to ensure equilibrium; achieving a stable and homogeneous state prior to energizing the reaction. The post-reaction gas is analyzed 10 min after the start of the reaction, followed by a subsequent analysis 20 min later. The reaction is deemed to have reached a stable state if no differences are observed between the two analyses, and data from the oscilloscope and spectrometer are recorded. In the case of the heating reaction, the heating rate is maintained at 10 °C/min, and the discharge reaction commences when the furnace temperature increases to 25 °C above the set temperature.

Power supply discharge power calculation method: Experiments reveal that the frequency of discharges required to achieve the same current varies when the gas composition is altered, indicating that the three discharge parameters do not remain entirely consistent across different operating conditions. Consequently, it becomes imperative to maintain consistent voltage and current levels to ensure uniform input power supply. Thus, the generation of Lissajous graphs, each encompassing 2.5 discharge cycles, becomes essential. The area of the Lissajous graphs can be utilized to compute the power output and efficiency using the following formulas:

$$P_{\text{out}} = f \times C \times k \times k_x \times k_y \times \frac{S}{2.5} \quad (1)$$

$$Q = \frac{P_{\text{out}}}{P_{\text{in}}} \times 100\% \quad (2)$$

$$P_{\text{in}} = UI \quad (3)$$

Where, f is the discharge frequency, C is the sampling capacitance, k is the voltage sampling attenuation multiplier, k_x and k_y are the total attenuation multiplier of CH1 and CH2 channels, respectively, U is the power input power, and I is the discharge current.

Methane and each gas product selectivity is calculated as follows:

Methane conversion is defined as the amount of methane converted as a percentage of the initial amount:

$$X_{\text{CH}_4} (\%) = \frac{n_{\text{CH}_4, \text{in}} - n_{\text{CH}_4, \text{out}}}{n_{\text{CH}_4, \text{in}}} \times 100\% \quad (4)$$

Hydrocarbon product selectivity is defined as the percentage of carbon atoms in the hydrocarbon to the carbon atoms of the converted methane:

$$S_{\text{C}_x\text{H}_y} = \frac{x n_{\text{C}_x\text{H}_y}}{n_{\text{CH}_4, \text{in}} - n_{\text{CH}_4, \text{out}}} \times 100\% \quad (5)$$

Hydrogen selectivity is defined as the number of H atoms in hydrogen as a percentage of the H in the CH₄ undergoing conversion:

$$S_{\text{H}_2} = \frac{n_{\text{H}_2}}{2 \times (n_{\text{CH}_4, \text{in}} - n_{\text{CH}_4, \text{out}})} \times 100\% \quad (6)$$

Where, $n_{\text{CH}_4, \text{in}}$ denotes the amount of imported methane, $n_{\text{CH}_4, \text{out}}$ denotes the amount of exported methane, $n_{\text{C}_x\text{H}_y}$ denotes the amount of a defined hydrocarbon product, and n_{H_2} denotes the amount of hydrogen produced.

Solid-phase product testing method-SEM: The solid products' particle size and structural morphology are observed using SEM, providing a two-dimensional surface distribution of carbon deposits and semi-quantitative information on the distribution of various elements within a specific range. The experiments are conducted with a Hitachi Regulus 8100 SEM, with the samples being ultrasonicated before the tests. An accelerating voltage of 20 kV is chosen to observe the sample morphology at varying magnifications.

Solid-phase product testing method-Raman: Raman spectroscopy is utilized to analyze the level of graphitization of solid-phase carbon products following cracking, as well as to examine the role of plasma in controlling the structural growth of methane-cracked carbon products. The experiment employs the HORIBA LabRAM HR Evolution, and the Raman spectra are analyzed using the DXR laser confocal micro-Raman spectrometer, employing a laser with a wavelength of 532.15 nm and a spectral range of 800–2000 cm⁻¹.

Spectral Intensity Calculation: In atomic emission spectroscopy theory, it is posited that in thermodynamic equilibrium or localized thermodynamic equilibrium, particles emit light of a specific wavelength as they transition from a higher to a lower energy state. In an examination of atomic or ionic spectra, it is essential to select two spectral lines from the same entity that fall within a comparable wavelength range. The radiation intensity of these chosen spectral lines should conform to formula (7), while their relative intensity needs to satisfy formula (8). By taking the logarithm of formula (8), the resulting equation is (9):

$$I = \frac{1}{4\pi} \frac{hc}{\lambda} AN \frac{g}{2} \exp\left(-\frac{E_k}{kT_e}\right) \quad (7)$$

$$\frac{I_1}{I_2} = \frac{A_1 g_1 \lambda_2}{A_2 g_2 \lambda_1} \exp\left(-\frac{E_1 - E_2}{kT_e}\right) \quad (8)$$

$$kT_e = (E_2 - E_1) \left[\ln\left(\frac{I_1 \lambda_1 A_2 g_2}{I_2 \lambda_2 A_1 g_1}\right) \right]^{-1} \quad (9)$$

Where, k represents the Boltzmann constant with a value of $1.38 \times 10^{-23} \text{ J K}^{-1}$; T_e stands for the electronic excitation temperature; h denotes Planck's constant; c signifies the speed of light in a vacuum; N denotes the total atomic number density; I_1 and I_2 are the relative spectral intensities of two spectral lines; A_1 and A_2 indicate the jump probabilities of particles; g_1 and g_2 stand for the statistical weights; λ_1 and λ_2 represent the wavelengths of the spectral lines; and E_1 and E_2 correspond to the excited state energies of each spectral line. Where, the values of E_k , g , and A can be obtained from the National Institute of Standards and Technology (NIST) Table of Leap Probabilities. Subsequently, the electronic excitation temperature can be computed by incorporating the pertinent parameters.

3. Results and discussion

3.1. Effect of Ar addition ratio on the reaction

To examine the impact of gas ratio changes on the reaction outcomes, the gas residence time and discharge parameters for every working condition are held constant. The total gas flow rate is stabilized at 30 sccm, and the reaction is conducted under conditions that doesn't

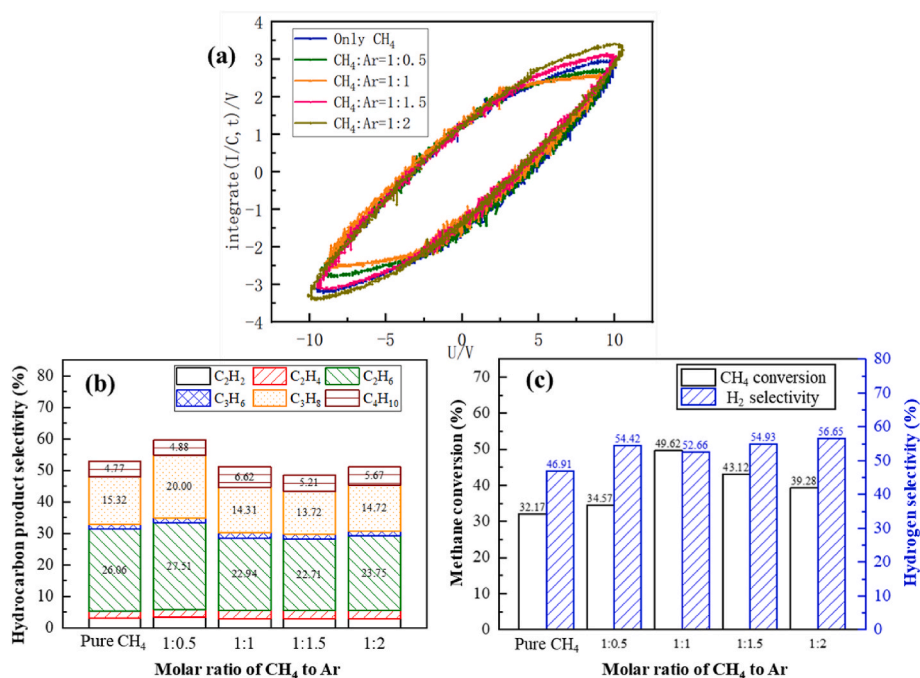


Fig. 2. Gas product results for different gas ratios: (a) Lissajous graphs; (b) Hydrocarbon product selectivity; (c) Methane conversion and hydrogen selectivity.

provide an additional heat source, maintaining at room temperature (25 °C). Furthermore, the plasma discharge power is set at 120W. The power supply efficiency can indicate the percentage of energy use for discharge and the rest of the energy is dissipated in the form of heat. Fig. 2(a) displays the Lissajous graphs representing the discharge with varying gas ratios. By analyzing each Lissajous graph, it is apparent that the power efficiency ranges from 34.6% to 40% in the order from the least to the highest proportion of Ar added for a specific power input. This suggests that the inclusion of Ar diminishes the power supply efficiency, with the lowest power supply efficiency occurring when the ratio of $\text{CH}_4:\text{Ar} = 1:1$, resulting in a 5.43% decrease compared to the pure methane condition. Fig. 2(b) shows the selectivity of hydrocarbon products under different Ar ratios, and it can be seen that the hydrocarbon products of CH_4 and CH_4/Ar under dielectric blocking discharge

are mainly C_2H_6 , C_3H_8 , C_4H_{10} , C_2H_2 , C_2H_4 , and C_3H_6 , and the cracking of CH_4 under the discharge conditions can be viewed as a process where CH_4 molecules are cleaved into molecular fragments and radicals, and then later radicals undergo recombination to the final process of generating a variety of hydrocarbon substances, while the free radical reaction course of generating ethane and propane is the shortest, and the energy required is lower, so its generation is more. At this time, the residence time of the gas in the plasma region is about 60 s, which can be regarded as the maximum reaction, and it is difficult to extend the residence time to make it completely cracked. The selectivity of C_2H_6 increases by 4.68% at $\text{CH}_4:\text{Ar} = 1:0.5$, and the selectivity of the rest of the hydrocarbon products did not change significantly. At $\text{CH}_4:\text{Ar}$ of 1:1, 1:1.5 and 1:2, respectively, the selectivity of each hydrocarbon fluctuates little, indicating that Ar does not affect the ratio of reactions

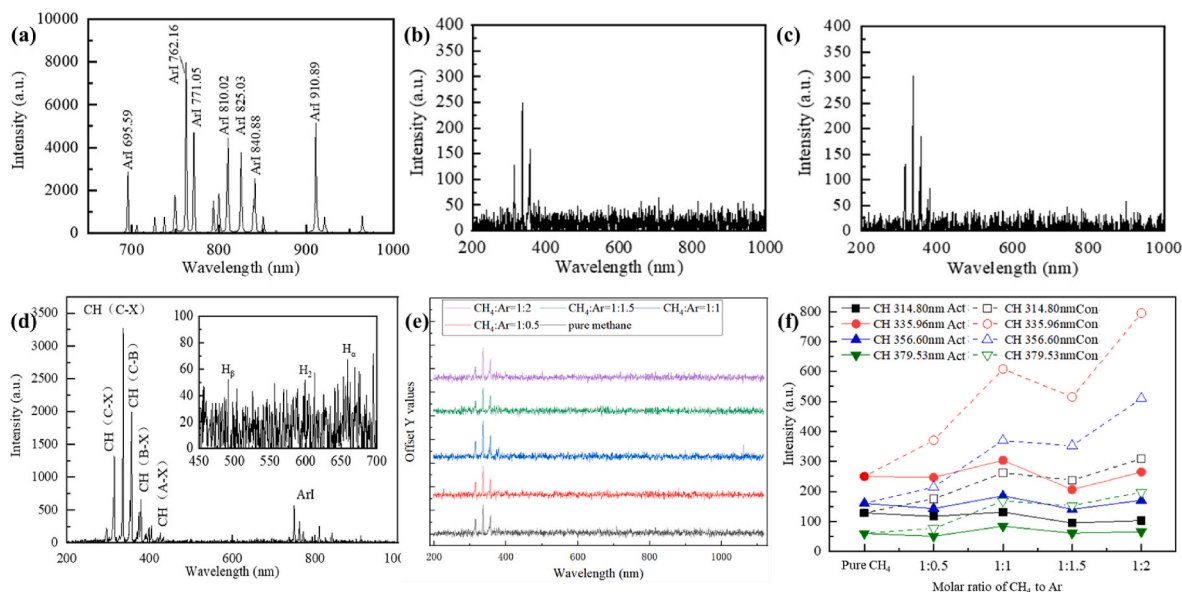


Fig. 3. (a) Spectrum analysis of Ar discharge; (b) Spectral line of CH_4 ; (c) Joint spectral line of CH_4 and Ar; (d) Spectrum analysis at elevated supply input power; (e) Spectral lines across varying gas ratios; (f) Comparison between actual and theoretical CH radical intensities across different gas ratios.

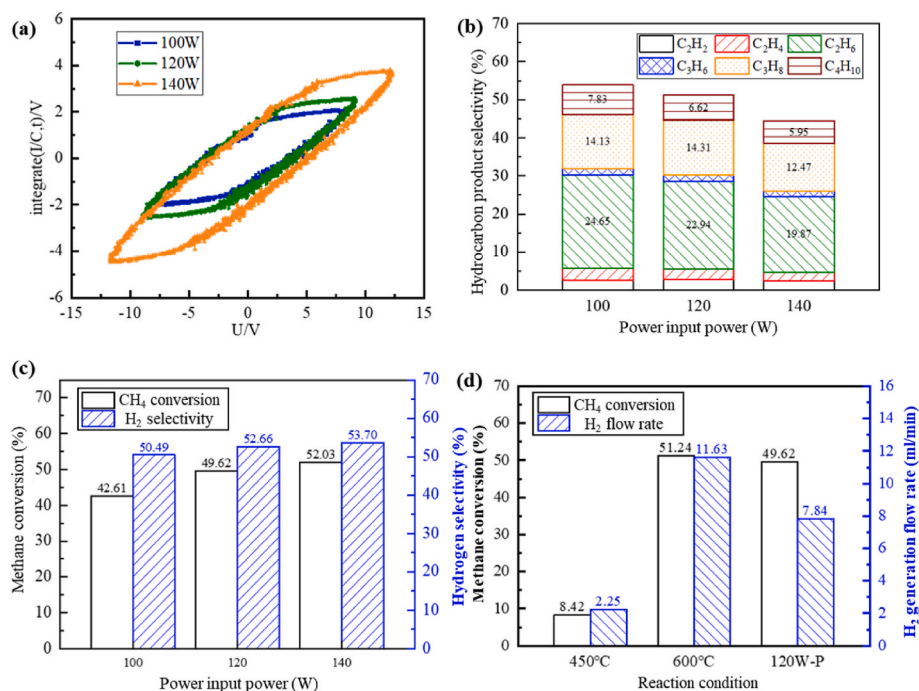


Fig. 4. The outcomes from the gas-phase product under varying power inputs: (a) Results from Lisaru Graphics; (b) Selectivity of hydrocarbon products; (c) Conversion rates and selectivity of CH_4 and H_2 respectively; (d) Comparative analysis of plasma-cracked CH_4 and thermally cracked CH_4 results.

occurring between carbon-containing radicals. Fig. 2(c) shows the methane conversion and hydrogen selectivity under different gas ratios. The conversion of CH_4 increases when Ar is added at four different ratios, and the H_2 selectivity is improved by the addition of Ar compared with that of pure methane [31]. In the pure methane state, the CH_4 conversion rate is 32.17%, and the H_2 selectivity is 46.91%; with the increase of Ar concentration, the CH_4 conversion rate shows a pattern of increasing and then decreasing, and the conversion rate reaches the highest 49.62% when the molar ratio is 1:1. The H_2 selectivity of the four Ar-containing cases are concentrated in the range of 52.66%–56.65%, and did not change drastically with the change of the ratio of Ar [32], indicating that Ar has less influence on the various pathways of H_2 generation and does not reflect the selectivity of H_2 .

Combining the aforementioned results regarding CH_4 discharge cracking for various Ar doping ratios, the introduction of Ar enhances methane conversion, primarily attributed to the Penning effect [33], leading to increased activation of CH_4 . The power supply efficiency experiences the most significant decrease [34], and the overall selectivity of C_2 – C_4 hydrocarbons is lower for CH_4 : Ar = 1:1, despite the peak CH_4 conversion occurring at this ratio. This can be attributed to the limited discharge energy input in the reactor, whereby a higher CH_4 ratio does not contribute the required energy for methane cracking [35]. Conversely, the proportion of Ar exceeding 50% results in diminished CH_4 conversion [36], potentially due to an increased concentration of Ar atoms and ions in the system, leading to reduced collisional scattering between electrons and methane molecules.

The grating spectrometer detects the intermediate products of plasma discharge. Fig. 3(a) displays the Ar plasma emission spectra, within which several prominent Ar I spectral lines are visible in the 690–920 nm range. These lines are produced by the $4p \rightarrow 4s$ transition of Ar atoms. Fig. 3(b) & (c) showcase the CH_4 and $\text{CH}^* + \text{Ar}$ spectra, respectively. In the CH_4 discharge [37,38], there are three significant spectral lines. Additionally, upon introducing Ar to the discharge, one can observe four notable spectral lines within the span of 300–400 nm. However, the intensity of the Ar lines significantly diminishes to the point of being challenging to discern. Fig. 3(d) shows the spectra when the input power is increased to more than 400 W. It can be seen that

there are four obvious spectral lines at 314.80 nm, 335.96 nm, 356.60 nm, and 379.53 nm, which correspond to the CH radical bands, and their spacings are basically equal [39]. H_α and H_β are observed at 655.99 nm and 485.83 nm, corresponding to the $n = 3 \rightarrow 2$ and $n = 4 \rightarrow 2$ processes of electrons, respectively, and their intensities are very low. This is due to the extremely short lifetime of the H radical, which can generate H_2 within 1×10^{-15} s. 603.02 nm corresponds to the H_2 molecule, although its intensity is also low, which is due to the fact that H_2 is a generator in the system, with a small relative content and a relatively high dissociation energy, which is not easy to decompose.

Fig. 3 (e) compares the intensity of the spectral lines in the range of 200–1000 nm for pure CH_4 , CH_4 : Ar of 1:0.5, 1:1, 1:1.5, and 1:2. The spectral peak positions in the distributions of the five distinct gas ratios exhibit a significant degree of similarity. Furthermore, only in the case of CH_4 does it present a relatively larger intensity of four spectral lines making it a challenge to distinguish the signal response of the Ar I band from the noise. This suggests that both the addition and the proportion of Ar do not substantially alter the intermediate active species. This further reinforces the conclusion that Ar proportional influence on the product selectivity is minimal [40]. Fig. 3(f) shows the intensity of CH^* radicals with gas ratio. The solid line in the figure shows the actual detected intensity values, which show a trend of increasing and then decreasing with increasing Ar ratio, reaching a peak at $\text{CH}_4/\text{Ar} = 1:1$, and the CH^* intensity decreases after the Ar ratio exceeds 50%. The dashed line in the figure shows the CH^* spectral intensity corresponding to converting the CH_4 in the gas mixture to the same content, which gradually increases with the increase in the proportion of Ar. This trend provides evidence that the addition of Ar effectively increases the number of free radicals dissociated from CH_4 molecules. Notably, weaker dissociation of CH_4 is observed when there is a lower proportion of Ar, resulting in a lower conversion rate. Conversely, a significant increase in the proportion of dissociated CH_4 is observed when there is an excess of Ar. However, due to the low proportion of free radicals, the dissociation occurs with Ar, leading to a decrease in CH^* intensity when the proportion of free radicals is lower [41]. When there is an excessive amount of Ar, the proportion of CH_4 dissociation significantly increases. However, this leads to a higher probability of collision with Ar after

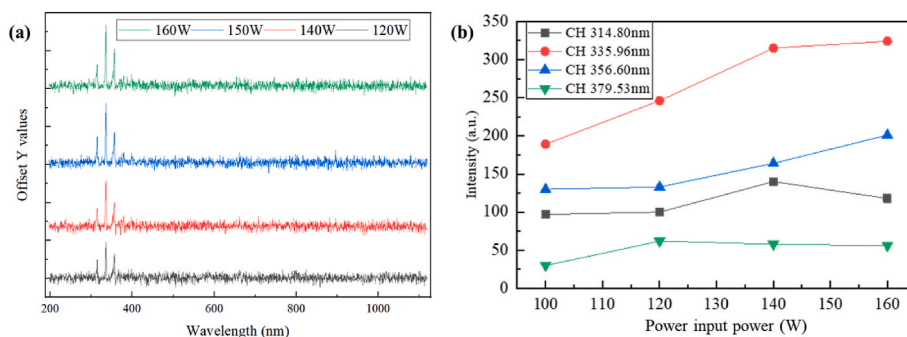


Fig. 5. (a) Spectral lines at different power inputs; (b) CH* radical intensity under different power supply.

dissociation, as there is a low proportion of radicals overall. This impedes the continuation of the reaction and results in a decrease in CH₄ conversion.

3.2. Effect of discharge power on the reaction

To examine the influence of the plasma power supply's discharge power, the CH₄: Ar ratio is maintained at 1:1. Moreover, the reaction temperature remains consistent without the addition of any external heat sources. Fig. 4(a) shows the graph of Lissajous for input power of 100 W, 120 W, and 150 W. The output power is 33.68 W, 41.49 W, and 71.78 W. The power supply efficiency is 33.68%, 34.57%, and 47.85%, and the power supply efficiency increases with the increase in power supply. This is due to the fact that an electron avalanche is triggered after the voltage exceeds the Paxing voltage [42], which leads to an exponential increase in the electron number density [43]. Therefore, the current increases rapidly with the voltage, which in turn leads to an increase in the power supply efficiency. The selectivity of H₂ products at different powers is shown in Fig. 4(b), and the highest selectivity of hydrocarbon products is observed for C₂H₆, C₃H₈ and C₄H₁₀, which are 24.65%, 14.13% and 7.83%, respectively, under 100 W conditions. The overall selectivity of C₂–C₄ hydrocarbon products gradually decreased with increasing discharge power. The corresponding methane conversion and hydrogen selectivity are shown in Fig. 4(c). The methane

conversion rate increases with increasing discharge power, indicating that high power is more advantageous to the process of CH₄ dissociation reaction, which is consistent with the theoretical prediction [44]. The hydrogen selectivity, on the other hand, did not change significantly with the power source, indicating that the increase in discharge power has basically the same degree of effect on the H₂ generation pathway within the reaction system [45], and does not reflect a specific selectivity for H₂. The hydrogen-carbon ratios of the six hydrocarbon products determined at different powers ranged from 2.64:1 to 2.67:1, which did not change significantly. The average hydrogen-carbon ratio of the remaining products ranged from 1.11 to 1.39 as shown by the analysis of methane conversion and atomic conservation of the known products. The yield of C₂H₂ is very low and included in the measured products, while the aromatization reaction of methane had a very low yield in the absence of a catalyst [46], and it is assumed that the decrease in hydrocarbon conversion when the power is increased is due to the increase in solid-phase carbon products after the conversion of CH₄.

Fig. 4(d) compares the conversion and hydrogen selectivity of plasma-cracked methane with those of thermally cracked methane under identical flow conditions. The thermal cracking reaction is conducted utilizing a 25% Ni/Al₂O₃ catalyst [47] at a volumetric gas flow rate of 18000·g_{Ni}⁻¹·h⁻¹ for CH₄, and CH₄ conversion and H₂ generation rates are selected as the comparative metrics since no gaseous byproducts other than H₂ are identified by chromatographic analysis. In the

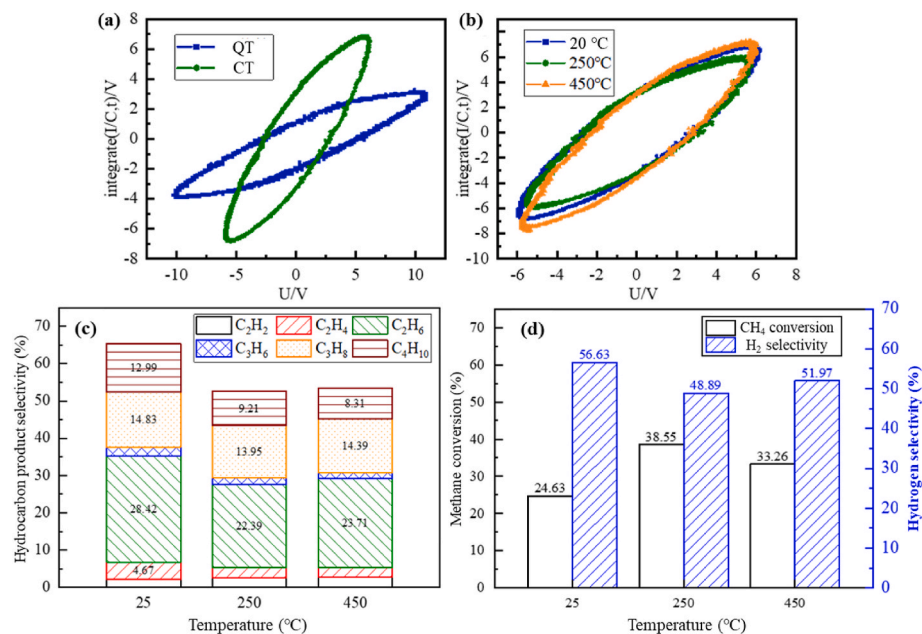


Fig. 6. (a) Lissajous graphs across various media; (b) Lissajous graphs at different temperatures; (c) Selectivity of hydrocarbon products at different temperatures; (d) Methane conversion and hydrogen selectivity at varying temperatures.

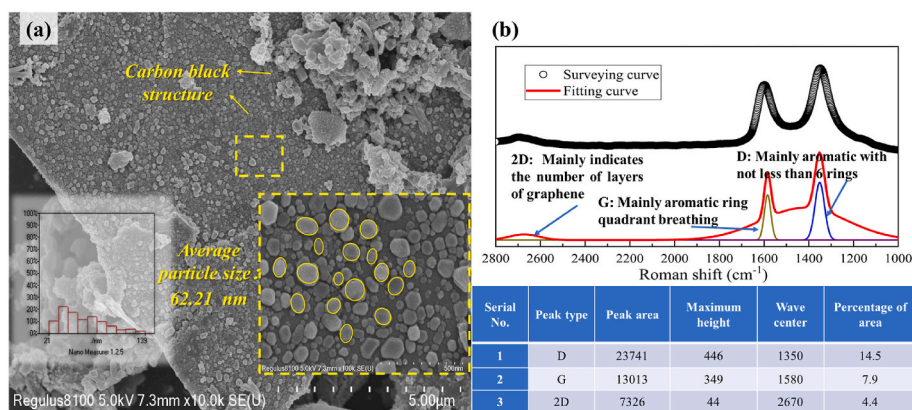


Fig. 7. (a) SEM characterization of solid-phase products in the presence of plasma; (b) Raman peak splitting and characterization results.

experimental study, it is observed that raising the temperature from 450 °C to 600 °C resulted in a significant increase in both methane conversion and hydrogen generation flow rate. Specifically, the methane conversion increases from 8.42% to 51.24%, while the hydrogen generation flow rate rose from 2.25 mL/min to 11.63 mL/min. These findings highlight the crucial influence of temperature on the efficiency of methane cracking reaction. When the temperature reaches 25 °C, with only the plasma contributing at a discharge intensity of 120 W, methane conversion rates reaches 54.59%, and the hydrogen generation flow rate reaches 7.84 mL/min, nearly equivalent to that of cracking at 600 °C. This underscores the pivotal role of plasma in catalyzing the reaction, demonstrating the promising economic viability of utilizing low-temperature plasma for methane cracking to produce H₂.

Fig. 5(a) presents the intensity of spectral lines within the range of 200–1000 nm for input powers of 100 W, 120 W, 140 W, and 160 W. Notably, the spectral peaks for CH* and Ar I occur in the same range, albeit at different discharge powers. While the positions of these spectral peaks remain similar across various discharge powers, it should be noted that the four spectral lines of CH* are markedly more intense, making the Ar I band relatively challenging to observe. Fig. 5(b) shows the variation of the intensity of CH- radicals with the discharge power. The intensity of each band of the CH* spectrum generally tends to increase as the power of the power supply rises [48]. The increase in power has a greater facilitating effect on the dissociation of methane molecules, which leads to more conversion of methane to radicals, but it affects the individual radical reactions to a similar extent, so there is no significant change in the selectivity of the products. From the point of view of H₂ generation, the highest yield at 120 W, the lowest energy consumption for converting unit of CH₄ and the lowest energy consumption for generating unit of H₂ in this study, which has the best techno-economy.

3.3. Effect of discharge temperature on the reaction

Fig. 6(a) shows the Lissajous-Figure of quartz and corundum tube discharges. It can be seen that the quartz tube needs a higher voltage to breakdown, which may be caused by the higher microscopic lattice ordering degree of corundum than that of quartz, and it can be seen that the power supply efficiency of the corundum tube is about 9% higher than that of the quartz tube after calculation. Fig. 6(b) shows the Lissajous-Figure for discharges at 25 °C, 250 °C and 450 °C. The power supply efficiencies are 43.67%, 39.91% and 40.32%, respectively, and the warming conditions cause a slight decrease in the power supply efficiency.

To quantify the influence of temperature on the plasma-induced cracking of methane, the discharge power of the power supply is maintained at 120 W, and since spectroscopic monitoring is not possible, the gas is fed into pure CH₄. Fig. 6(c) shows the selectivity of each hydrocarbon product after CH₄ conversion at 25 °C, 250 °C and 450 °C. It

can be seen that the main hydrocarbon products are C₂H₆, C₃H₈, and C₄H₁₀, with selectivity of 28.42%, 14.83%, and 12.99% at 25 °C. After increasing the temperature to 250 °C, the selectivity of C₂–C₄ hydrocarbons are reduced, among which the selectivity of C₂H₆ is reduced by 6.01%, and the selectivity of C₄H₁₀ is reduced by 3.78%, which proved that the increase of temperature could make the double CH₃* radical binding reaction weakened; continuing to increase the temperature to 450 °C, the selectivity of the hydrocarbons is found to be slightly increased, but the overall change is not significant, which indicates that in the presence of plasma, elevated temperatures resulted in a decrease in the selectivity of hydrocarbons in the products compared to ambient temperatures [49], but the difference between 250 °C and 450 °C is not significant. The hydrogen-carbon ratios of the remaining products ranged from 1.08 to 1.39, and the coverage of carbon products on the surface of the electrode at the end of the warming reaction is enhanced compared with that at 25 °C. Fig. 6(d) shows the methane conversion and hydrogen selectivity during discharge at three temperatures, and the methane conversion is 24.63%, 38.55% and 33.26% at 25 °C, 250 °C and 450 °C, respectively, which shows that the temperature has a large influence on the reaction activity, and when the temperature is raised from 25 °C to 250 °C, the cleavage reaction is obviously promoted, and the methane conversion rate is significantly increased. However, when the temperature is raised to 450 °C, the methane conversion rate decreased. The hydrogen selectivity is 56.63%, 48.89% and 51.97% at the three temperatures, respectively, which decreases with increasing temperature, indicating that the temperature did not reflect the selectivity for the H radical combination to generate H₂ [50]. It is also possible that this is due to the energy limitation of the conversion process, where the conversion of methane to H₂ requires more C–H bonds to be broken, resulting in a slight decrease in H₂ selectivity when the methane conversion rate is increased [51]. Combining the methane conversion efficiency, energy consumption, and the yield of the product, 250 °C is the optimal reaction temperature among the three temperatures for the conversion of CH₄ to H₂.

3.4. Characterization of solid-phase carbon products

In the experimental conditions conducted, it is observed that only under plasma conditions, a thin layer of black solid forms on the high-pressure stainless-steel electrode after methane cracking, resulting in a very low yield. This layer is subsequently collected and characterized using scanning electron microscopy (SEM) and Raman spectroscopy. Fig. 7(a) illustrates that the solid-phase product is primarily composed of a carbon black structure, exhibiting morphology in both aggregated and dispersed states. The dispersed carbon black is uniformly distributed on the dispersant's surface in the form of irregular "carbon spheres." The average particle size of the dispersant, as determined from measurements, is 62.21 nm, indicating that plasma-induced electron

Table 1
Parameters of Raman spectral splitting [55].

Peak Type	Position (cm ⁻¹)	Description of Raman Spectral Peaks	Hybridization Type
G	1580	Ordered graphite C–C, CNTs and aromatic hydrocarbons with benzene rings	sp ²
D	1350	Amorphous carbon atoms C=C	sp ³
2D	2670	Edge structure, number of sheet layers	sp ³

bombardment typically results in a finer-grained distribution of the solid-phase product. Carbon black with fine particles holds significant application value, thus highlighting its importance for the high-value utilization of solid-phase products from methane plasma reforming reactions. Raman spectra of the solid products under examination are presented in Fig. 7(b). It is evident from the spectra that the prominent peaks occur at 1350 cm⁻¹ and 1580 cm⁻¹, corresponding to the disordered structure of carbon (D peak) and the graphitized structure of carbon (G peak) [52]. The intensity of the G peak is smaller than that of the D peak, indicating the generation of more inert carbon during the process, confirming its composition as carbon black. This finding aligns well with the SEM results described above. The value of the I_D/I_G ratio is determined by the area of specific Raman peaks in the sample, which hold significant meaning in representing the disordered structure of the carbon black [53]. Some studies have indicated that an increase in the disordered structure of the carbon corresponds to an increase in its active structure [54]. The I_D/I_G ratio of the current material is 1.83, indicating a high level of disorder, and the sample exhibits a diverse structure with inert functional groups. Furthermore, the ratio of the second-order Raman characteristic 2D peak (2670 cm⁻¹), I_{2D}/I_G is determined to be 0.55, suggesting the presence of graphene flakes with fewer layers (see Table 1). This indicates that the degree of graphitization in carbon black products can be modulated by altering the plasma voltage alongside other processes. Concurrently, with carbon black derived from plasma-induced solid-phase products lacking issues concerning the catalyst's separation, it showcases heightened purity. This aspect holds promising potential for applications in the rubber, plastic, and oil industries, warranting further investigation to tailor and streamline its specific functions.

4. Plasma-induced CH₄ cracking pathway analysis

The molecular structure of methane, renowned for its stability and difficult cracking process, has its thermodynamic equilibrium components calculated using a zero-dimensional reaction kinetic model in the Chemkin software. Within the temperature range of 800–2000 K, the thermodynamic equilibrium of methane's single-phase system, as determined by the GRIMech3.0 mechanism, is illustrated in Fig. 8(a). The typical temperature range employed for methane's catalytic cracking is approximately 800 K–1100 K. At 1000 K, the rate of methane cracking is only about 8%, while the production of H₂, C₂H₆, C₂H₄, C₂H₂, and C₃H₈ among the by-products is significantly low. Beyond 1600 K, the primary products in the equilibrium system are H₂ and C₂H₂, with CH₃^{*} and H^{*} being the main radicals. Based on the findings of the literature review, it is reasonable to propose that the plasma enhances the electronic reactions, thereby boosting the generation of free radicals. These radicals then combine to form each product molecule, as depicted in Fig. 8(b)&(c).

The application of plasma enables high-energy reactions at low temperatures, significantly enhancing the cracking efficacy of CH₄ through plasma induction. This process operates by facilitating the systematic fracture of the C–H bond, exciting it into CH^{*} and H^{*} radicals. Subsequently, these radicals reassemble into hydrocarbon molecules. Plasma induction can optimize the production of H₂ molecules and solid-phase carbon black without the need for additional heat sources. A discharge power of 120 W and a CH₄/Ar ratio of 1:1 generate optimal pathways for hydrogen production via methane cracking. However, in an atmosphere of pure CH₄, the judicious addition of an external heat source can supplant Ar for radical excitation. Under these conditions, the most energy-efficient reaction parameters involve 120 W and a temperature of 250 °C.

5. Conclusion

- (1) At a molar ratio of 1:1 between CH₄ and Ar, the methane CH₄ reaches its peak at 49.62%, with a H₂ selectivity of 52.66%. The selectivity towards primary hydrocarbon products, namely C₂H₆, C₃H₈, and C₄H₁₀, is 22.94%, 14.31%, and 6.62%, respectively.

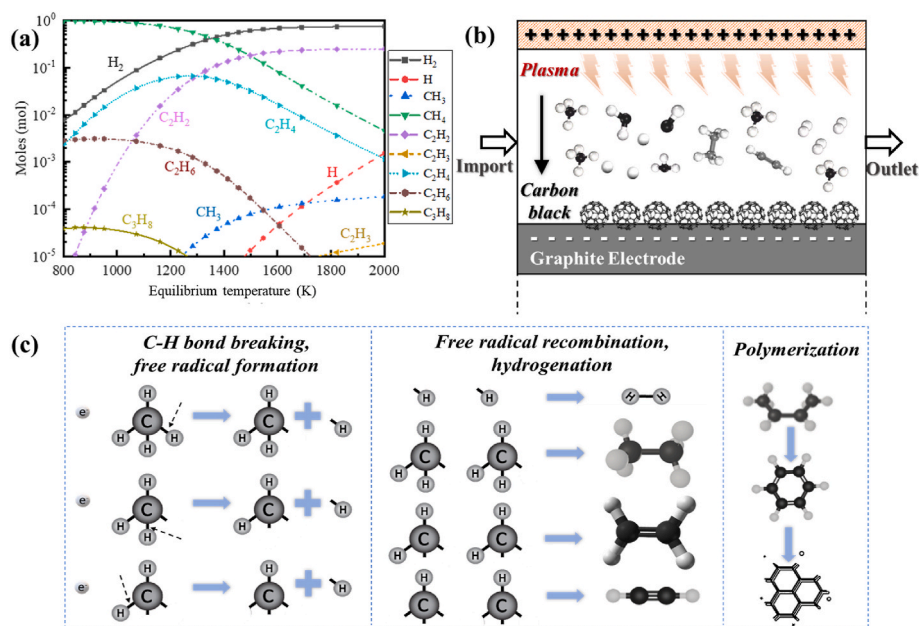


Fig. 8. (a) the equilibrium of a single-phase system for methane cracking at temperatures ranging from 800 to 2000 K; (b) the reaction mechanism for plasma-induced methane vapor deposition; (c) a schematic diagram illustrating the mechanism of plasma methane cracking.

The solid products have been characterized as carbon black, exhibiting an average particle size of around 62.21 nm.

- (2) An escalation in discharge power and temperature can enhance methane conversion, as evidenced by the increased CH* radical signals observed during the reaction. Operating at 250 °C and 120 W, this discharge exhibits significant practical value, leading to elevated methane conversion and hydrogen selectivity levels of 38.55% and 48.89%, respectively.
- (3) Temperature shows no significant influence on the selectivity of H radical binding to produce H₂. As the rate of methane conversion increases, a greater number of C–H bonds need to be broken to generate H, consequently leading to a slight decrease in H₂ selectivity.

Declaration of competing interest

The authors declare that they have no known competing financial interests or personal relationships that could have appeared to influence the work reported in this paper.

Acknowledgments

This work is supported by National Natural Science Foundation of China (52276180), Ministry of Education's "Chunhui Plan" Collaborative Research Project (HZKY20220318), Heilongjiang Province Natural Science Foundation (YQ2022E026) and Fundamental Research Funds for the Central Universities (2022ZFJH004).

References

- [1] Ashik UPM, Daud W, Abbas HF. Production of greenhouse gas free hydrogen by thermocatalytic decomposition of methane - a review. *Renewable & Sustainable Energy Reviews* 2015;44:221–56.
- [2] Zou C, Li J, Zhang X, Jin X, Xiong B, Yu H, et al. Industrial status, technological progress, challenges, and prospects of hydrogen energy. *Nat Gas Ind B* 2022;9:427–47.
- [3] Lu C, Venevsky S, Cao S. The effects of the China–Russia gas deal on energy consumption, carbon emission, and particulate matter pollution in China. *npj Climate and Atmospheric Science* 2018;1:8.
- [4] Hiraoka K, Aoyama K, Morise K. A study of reaction mechanisms of methane in a radio-frequency glow discharge plasma using radical and ion scavengers. *Can J Chem* 1985;63:2899–905.
- [5] Xu S, Whitehead JC, Martin PA. CO₂ conversion in a non-thermal, barium titanate packed bed plasma reactor: the effect of dilution by Ar and N₂. *Chem Eng J* 2017;327:764–73.
- [6] Chirokov A, Gutsol A, Fridman A. Atmospheric pressure plasma of dielectric barrier discharges. *Pure Appl Chem* 2005;77:487–95.
- [7] Claire Tendero, Christelle Tixier, et al. Atmospheric pressure plasmas: a review. *Spectrochimica Acta Part B Atomic Spectroscopy*; 2006.
- [8] Li XC, Zhao HH, Jia PY, Bao WT. A large gap uniform discharge excited by a direct-current voltage at atmospheric pressure. *Appl Phys Lett* 2013;102.
- [9] Li XC, Bao WT, Chu JD, Zhang PP, Jia PY. A uniform laminar air plasma plume with large volume excited by an alternating current voltage, vol. 24. *PLASMA SOURCES SCIENCE & TECHNOLOGY*; 2015.
- [10] Thanyachotpaiboon K, Chavadej S, Caldwell TA, Lobban LL, Mallinson RG. Conversion of methane to higher hydrocarbons in AC nonequilibrium plasmas. *AIChE J* 1998;44:2252–7.
- [11] Kado S, Sekine Y, Nozaki T, Okazaki K. Diagnosis of atmospheric pressure low temperature plasma and application to high efficient methane conversion. *Catal Today* 2004;89:47–55.
- [12] Li XS, Lin CK, Shi C, Xu Y, Wang YN, Zhu AM. Stable kilohertz spark discharges for high-efficiency conversion of methane to hydrogen and acetylene. *J Phys Appl Phys* 2008;41.
- [13] Nozaki T, Okazaki K. Innovative methane conversion technology using atmospheric pressure non-thermal plasma. *J Jpn Petrol Inst* 2011;54:146–58.
- [14] Indarto A, Choi JW, Lee H, Song HK. Effect of additive gases on methane conversion using gliding arc discharge. *Energy* 2006;31:2986–95.
- [15] Putra AEE, Nomura S, Mukasa S, Toyota H. Hydrogen production by radio frequency plasma stimulation in methane hydrate at atmospheric pressure. *Int J Hydrogen Energy* 2012;37:16000–5.
- [16] Jasinski M, Czyłkowski D, Hrycak B, Dors M, Mizeraczyk J. Atmospheric pressure microwave plasma source for hydrogen production. *Int J Hydrogen Energy* 2013;38:11473–83.
- [17] Redondo AB, Troussard E, van Bokhoven JA. Non-oxidative methane conversion assisted by corona discharge. *Fuel Process Technol* 2012;104:265–70.
- [18] Dong LF, He YF, Yin ZQ, Chai ZF. Hexagon and stripe patterns in dielectric barrier streamer discharge. *Plasma Sources Sci Technol* 2004;13:164–5.
- [19] Liu CJ, Xu GH, Wang TM. Non-thermal plasma approaches in CO₂ utilization. *Fuel Process Technol* 1999;58:119–34.
- [20] Istadi, Amin NAS. Co-generation of synthesis gas and C₂₊ hydrocarbons from methane and carbon dioxide in a hybrid catalytic-plasma reactor: a review. *Fuel* 2006;85:577–92.
- [21] Li SK, Ahmed R, Yi YH, Bogaerts A. Methane to methanol through heterogeneous catalysis and plasma catalysis. *Catalysts* 2021;11.
- [22] Guo ZF, Yi YH, Wang L, Yang JH, Guo HC. Pt/TS-1 catalyst promoted C-N coupling reaction in CH₄-NH₃ plasma for HCN synthesis at low temperature. *ACS Catal* 2018;8:10219. –+.
- [23] Liu M, Yi YH, Wang L, Guo HC, Bogaerts A. Hydrogenation of carbon dioxide to value-added chemicals by heterogeneous catalysis and plasma catalysis. *Catalysts* 2019;9.
- [24] Wang L, Yi Y, Chunfei W, Guo H, Tu X. One-step reforming of CO₂ and CH₄ into high-value liquid chemicals and fuels at room temperature by plasma-driven catalysis. *Angew Chem Int Ed* 2017;56.
- [25] Park J, Henins I, Herrmann HW, Selwyn GS, Jeong JY, Hicks RF, et al. An atmospheric pressure plasma source. *Appl Phys Lett* 2000;76:288–90.
- [26] Eliasson B, Kogelschatz U. Modeling and applications of silent discharge plasmas. *IEEE Trans Plasma Sci* 1991;19:309–23.
- [27] Gao N, Cheng M, Quan C, Zheng Y. Syngas production via combined dry and steam reforming of methane over Ni-Ce/ZSM-5 catalyst. *Fuel* 2020;273:117702.
- [28] Khalifeh O, Mosallanejad A, Taghvaei H, Rahimpour MR, Shariati A. Decomposition of methane to hydrogen using nanosecond pulsed plasma reactor with different active volumes, voltages and frequencies. *Appl Energy* 2016;169:585–96.
- [29] Ou Z, Ran J, Niu J, Zhang Z, Deng T, He Z, et al. Effect of active site and charge transfer on methane dehydrogenation over different Co doped Ni surfaces by density functional theory. *Int J Hydrogen Energy* 2020;45:31849–62.
- [30] De Bie C, Verheyde B, Martens T, van Dijk J, Paulussen S, Bogaerts A. Fluid modeling of the conversion of methane into higher hydrocarbons in an atmospheric pressure dielectric barrier discharge. *Plasma Process Polym* 2011;8:1033–58.
- [31] Liang C, Hu X, Wei T, Jia P, Zhang Z, Dong D, et al. Methanation of CO₂ over Ni/Al₂O₃ modified with alkaline earth metals: impacts of oxygen vacancies on catalytic activity. *Int J Hydrogen Energy* 2019;44:8197–213.
- [32] Zhang B, Chen Y, Kang B, Qian J, Chuai X, Peng R, et al. Hydrogen production via steam reforming of coke oven gas enhanced by steel slag-derived CaO. *Int J Hydrogen Energy* 2020;45:13231–44.
- [33] Jo S, Hoon Lee D, Seok Kang W, Song Y-H. Methane activation using noble gases in a dielectric barrier discharge reactor. *Phys Plasmas* 2013;20.
- [34] Zhu Q, Xu S, Sun J, Li X, Zhou D. Energy efficiency evaluation of power supply system: a data-driven approach based on shared resources. *Appl Energy* 2022;312:118683.
- [35] Busch P, Kendall A, Lipman T. A systematic review of life cycle greenhouse gas intensity values for hydrogen production pathways. *Renew Sustain Energy Rev* 2023;184:113588.
- [36] Taifan W, Baltrusaitis J. CH₄ conversion to value added products: potential, limitations and extensions of a single step heterogeneous catalysis. *Appl Catal B Environ* 2016;198:525–47.
- [37] Zhang S, Zeng X, Bai H, Zhang C, Shao T. Optical emission spectroscopy measurement of plasma parameters in a nanosecond pulsed spark discharge for CO₂/CH₄ dry reforming. *Spectrochim Acta Mol Biomol Spectrosc* 2022;267:120590.
- [38] Wang X, Gao Y, Zhang S, Sun H, Li J, Shao T. Nanosecond pulsed plasma assisted dry reforming of CH₄: the effect of plasma operating parameters. *Appl Energy* 2019;243:132–44.
- [39] Karmani S, Dunn-Rankin D. Visualizing CH* chemiluminescence in sooting flames. *Combust Flame* 2013;160:2275–8.
- [40] O'Brien TA, Wehner MF, Payne AE, Shields CA, Rutz JJ, Leung LR, et al. Increases in future AR count and size: overview of the ARTMIP tier 2 CMIP5/6 experiment. *J Geophys Res Atmos* 2022;127:e2021JD036013.
- [41] Marcus RA. Unimolecular dissociations and free radical recombination reactions. *J Chem Phys* 2004;20:359–64.
- [42] Cooray V, Cooray G. Electromagnetic radiation field of an electron avalanche. *Atmos Res* 2012;117:18–27.
- [43] Zalikhonov BZ. Critical point for transition of an electron avalanche to a streamer. *Phys Part Nucl Lett* 2023;20:84–95.
- [44] Zhao G-B, John S, Zhang J-J, Wang L, Muknahallipatna S, Hamann JC, et al. Methane conversion in pulsed corona discharge reactors. *Chem Eng J* 2006;125:67–79.
- [45] Khadir N, Khodja K, Belasri A. Methane conversion using a dielectric barrier discharge reactor at atmospheric pressure for hydrogen production. *Plasma Sci Technol* 2017;19:095502.
- [46] Zhang Z, Hu X, Wang Y, Hu S, Xiang J, Li C, et al. Regulation the reaction intermediates in methanation reactions via modification of nickel catalysts with strong base. *Fuel* 2019;237:566–79.
- [47] Xu Y, Du X, Shi L, Chen T, Wan H, Wang P, et al. Improved performance of Ni/Al₂O₃ catalyst deriving from the hydrotalcite precursor synthesized on Al₂O₃ support for dry reforming of methane. *Int J Hydrogen Energy* 2021;46:14301–10.
- [48] Kojima J, Ikeda Y, Nakajima T. Spatially resolved measurement of OH*, CH*, and C₂* chemiluminescence in the reaction zone of laminar methane/air premixed flames. *Proc Combust Inst* 2000;28:1757–64.
- [49] Kongpraves G, Wongsawaeng D, Ngaosuwan K, Kiatkittipong W, Assabumrungrat S. Low-temperature and atmospheric pressure plasma for palm biodiesel hydrogenation. *Sci Rep* 2021;11:14224.

- [50] Zhang K, Zhan Z, Zhu M, Lai H, He X, Deng W, et al. An efficient electrocatalytic system composed of nickel oxide and nitroxyl radical for the oxidation of bio-platform molecules to dicarboxylic acids. *J Energy Chem* 2023;80:58–67.
- [51] Li X, Li C, Xu Y, Liu Q, Bahri M, Zhang L, et al. Efficient hole abstraction for highly selective oxidative coupling of methane by Au-sputtered TiO₂ photocatalysts. *Nat Energy* 2023;8:1013–22.
- [52] Mintz KJ, Bartoli M, Rovere M, Zhou Y, Hettiarachchi SD, Paudyal S, et al. A deep investigation into the structure of carbon dots. *Carbon* 2021;173:433–47.
- [53] Potgieter-Vermaak S, Maledi N, Wagner N, Van Heerden JHP, Van Grieken R, Potgieter JH. Raman spectroscopy for the analysis of coal: a review. *J Raman Spectrosc* 2011;42:123–9.
- [54] Wang B, Sun L, Su S, Xiang J, Hu S, Fei H. Char structural evolution during pyrolysis and its influence on combustion reactivity in air and oxy-fuel conditions. *Energy Fuels* 2012;26:1565–74.
- [55] Wu A, Li X, Yan J, Yang J, Du C, Zhu F, et al. Co-generation of hydrogen and carbon aerosol from coalbed methane surrogate using rotating gliding arc plasma. *Appl Energy* 2017;195:67–79.